

Crystallization of Isotactic Polypropylene under the Spatial Confinement Templated by Block Copolymer Microdomains

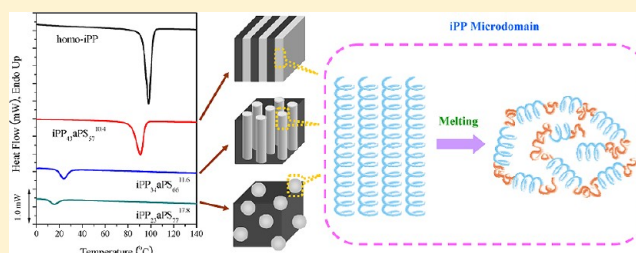
Ming-Champ Lin,[†] Hsin-Lung Chen,^{*,†} Wen-Fu Lin,[‡] Pei-Sun Huang,[‡] and Jing-Cherng Tsai[‡]

[†]Department of Chemical Engineering and Frontier Center of Fundamental and Applied Sciences of Matters, National Tsing Hua University, Hsin-Chu 30013, Taiwan

[‡]Department of Chemical Engineering, National Chung Cheng University, Chia-Yi 62142, Taiwan

S Supporting Information

ABSTRACT: We investigate the crystallization behavior of isotactic polypropylene (iPP) under the influence of nanoscale confinement templated by the microphase-separated structure of an iPP-based diblock copolymer system, isotactic polypropylene-*block*-atactic polystyrene (iPP-*b*-aPS). Three types of iPP microdomains, i.e., lamellae, cylinder, and sphere, were generated by controlling the composition of the diblock. The effect of microdomain morphology on the nucleation mechanism, crystallization kinetics, self-nucleation behavior, the population of the helical sequence of iPP block in the melt state, and crystal orientation have been systematically studied. It was found that the crystallization rate of iPP was predominantly controlled by homogeneous nucleation when the crystallization process was largely confined within the individual cylindrical and spherical microdomains. Such a nucleation mechanism and the highly frustrated crystal growth in the isolated microdomains led to the absence of Domain II and atypical crystallization kinetics in Domain III in the self-nucleation study. The population of the longer helical sequence of iPP block revealed by infrared spectroscopy was found to be affected by temperature but not by the spatial confinement, chain stretching, and junction point constraint imposed by the microdomains. Finally, the orientation of α -form iPP crystals in the lamellae-forming iPP-*b*-aPS was identified over a broad range of crystallization temperatures (T_c). Different from other crystalline–amorphous diblocks, a lamellar branching of α -form iPP was observed in the lamellar microdomains at T_c lying between 15 and 80 °C, where the daughter lamellae developed from the perpendicularly orientated parent iPP crystals with a specific angle of 80° or 100°. Once the sample was crystallized at $T_c \leq 10$ °C, the iPP crystals became randomly oriented.



1. INTRODUCTION

Self-assembly of diblock copolymer can generate a series of long-range ordered microdomains, depending on the volume fraction of the constituting blocks and the segregation strength denoted by χN (where χ is the Flory–Huggins interaction parameter and N is the overall chain length).^{1–3} Since the dimension of the microdomain is prescribed by the radius of gyration of the block chains, these domains offer convenient nanoscale templates wherein the dynamics and structural changes associated with the phase transformation may be drastically different from those in the bulk homopolymer.

Incorporation of one crystallizable block into diblock copolymer system, which is termed crystalline–amorphous (C–A) diblock copolymer, generates a special type of materials exhibiting the hierarchical structure generated by the interplay between microphase separation (yielding long-range ordered arrangement of the microdomains on a larger length scale) and crystallization (leading to the ordering of chains at the molecular level). The crystallization-mediated structure formation in C–A diblock copolymers has been investigated extensively. It has been established that the interblock segregation strength, the order–disorder transition temperature

(T_{ODT}), the crystallization temperature of C block (T_c), and the glass transition temperature of A block (T_g^A) are the main factors governing the extent of confinement to the crystallization process. When $T_c < T_g^A < T_{ODT}$ (where the A phase is in the glassy state upon crystallization process), the crystallization of C block can be effectively confined within the microdomains prescribed by the microphase separation.^{4–8} If $T_g^A < T_c < T_{ODT}$, the amorphous phase constituted by A block remains soft during crystallization of C block; in this case, the extent of perturbation of the melt mesophase by crystallization is dependent on the segregation strength of the system.^{6–12}

Several intriguing features associated with the crystallization in C–A diblock copolymers have been identified. When C block is the majority component, it forms a continuous phase in the melt; the crystallization behavior of C block is thus similar to that in the homopolymer in the sense that the crystal growth may propagate continuously over a macroscopic length scale. If

Received: June 29, 2012

Revised: August 17, 2012

Published: August 22, 2012

C and A blocks are of similar proportion or when C block becomes the minority constituent, the microdomain formed by C may impose nanoscale confinement to frustrate the crystal growth. In this case, a distinct correlation between the microdomain morphology and the crystallization kinetics has been identified.^{13–15} It was further observed that, when the crystallization was isolated within the cylindrical and spherical microdomains, the overall crystallization kinetics of the systems was dominated by the homogeneous nucleation because the microdomains greatly outnumber the heterogeneous nuclei.^{13–15} Most studies concerning the correlation between crystallization kinetics and microdomain morphology so far have focused on the C-A diblocks with polyethylene oxide (PEO), polyethylene (PE), or poly(ϵ -caprolactone) (PCL) as the C block.^{5,13–15} A similar issue has not been addressed in detail for the C-A system whose C block is stereoregular in nature.¹⁶ In this study, we introduce a stereoregular C-A diblock copolymer comprising an isotactic polypropylene block and an atactic polystyrene block (i.e., iPP-*b*-aPS) to systematically explore the confinement effect on the crystallization behavior and local conformational structure of iPP.

Stereoregular iPP is known to adopt a 3/1 helical conformation (TGTG) in the crystalline state.¹⁷ Such a helical structure can be conveniently identified by Fourier-transform infrared spectroscopy (FTIR). In the IR spectra of crystalline polymers, some absorption bands are sensitive to the local conformation or packing state of the chains. These sensitive bands can be classified into two categories: one of which is often termed the crystallinity band, which originates from the intermolecular coupling in the crystal lattice; the other is called the regularity band or helical band, which is connected with the intramolecular coupling of the oscillations of various atomic groups. The helical bands associated with different lengths of the helical sequence have been identified for iPP homopolymers.^{18–21} However, the population of helical sequence in iPP-based block copolymer in which the iPP blocks are confined within the microdomains has not been reported so far. Comparing to the homopolymer, the microphase separation in block copolymer would induce the chains to stretch normal to the interface. When the volume fraction of a constituent greatly deviates from 0.5, the conformational entropy loss caused by the stretching of the majority block overwhelms the penalty of forming curved interface. This then drives a transition of microdomain morphology from lamellae to the ones with a curved interface (i.e., cylinder or sphere), and the minority blocks become more stretched, normal to the interface with increasing interfacial curvature. On the basis of this idea, we intend to unravel if the chain stretching induced by the microdomain structure would enhance the stability of the longer helical sequence in the iPP block in the melt state. This may provide significant insight into the correlation between the global chain stretching and the local conformational structure of the stereoregular chains in the diblock copolymer.

In addition to crystallization kinetics, the preferential orientation of the crystals formed in the lamellar microdomains of C-A diblock copolymers has also received considerable attention in the past decade. The PEO-, PE-, PLLA-, and PCL-containing diblocks have been widely used as the model systems to investigate this problem. Perpendicular orientation (where the crystalline stems orient perpendicularly to the lamellar interface) was frequently observed for the PEO-, PLLA-, and PCL-based systems at the normal degree of undercooling;^{6,22–25} however, the PE-containing diblocks

seemed to behave anomalously, in that the crystals usually showed parallel orientation (with the crystalline stems aligning parallel to the lamellar interface).^{11,26–28} Several parameters have been found to affect the crystal orientation in C-A diblocks,²⁹ including crystallization temperature,³⁰ confinement size,^{31,32} and reduced tethering density,³³ whereas the confinement type (soft or hard confinement)^{6,28} and the nucleation mechanism^{33,34} did not play a role in the final crystal orientation. Since the crystal orientation in iPP-based C-A diblocks has not been investigated, it is of interest to examine the orientation of iPP crystals in iPP-*b*-aPS and compare the result with those of the previously studied C-A systems.

In this study, we investigate the dependence of crystallization kinetics on the microdomain structure of iPP-*b*-aPS. The self-nucleation experiment was carried out systematically to reveal the self-nucleation behavior in different types of microdomains. The influence of microdomain morphology on the population of the helical sequence of iPP block was also evaluated. Finally, the orientation of α -form iPP crystals in a lamellae-forming iPP-*b*-aPS was studied over a broad range of T_c . It will be shown that a special lamellar branching behavior of α -form iPP crystal still persisted even when the crystallization was confined in the lamellar microdomains.

2. EXPERIMENTAL SECTION

2.1. Materials. **2.1.1. General Procedure.** All reactions and manipulations were conducted under a nitrogen atmosphere using the standard Schlenk line or drybox techniques. Solvents and common reagents were commercially obtained and were used either as received or purified by distillation with sodium/benzophenone. Propylene (purity >99.95%) and oxygen (purity >99.5%) were obtained from Matheson and were used as received. *N*-Butyllithium (1.6 M in hexane) and *p*-toluenesulfonyl chloride (99%) were purchased from Aldrich and were used as received. The styrene (99%), purchased from Aldrich, was dried over calcium hydride and distilled under vacuum before use. $C_2H_4(Ind)_2ZrCl_2(III)$, purchased from Aldrich, was used as received. Triethylaluminum (TEA, 1 M solution in hexane), purchased from Aldrich, was used as received. Methylaluminoxane (MAO, 14% in toluene), purchased from Albemarle, was dried under vacuum to remove residual TMA.³⁵ The resulting TMA-free MAO was diluted in toluene to the desired concentration before use. The tosyl group end-capped iPP was synthesized by tosylation of OH-capped iPP using the method described in the literature.³⁶ The OH-capped iPP was synthesized in two steps: first, alkylaluminum end-capped iPP was generated via selective chain transfer to TEA mediated by isospecific metallocene catalyst; second, the resulting alkylaluminum end-capped iPP was in situ treated with O_2/H_2O_2 to generate OH-capped iPP with high yield.^{36,37}

2.1.2. Preparation of iPP-*b*-aPS. Here, we use iPP-*b*-aPS ($M_{n,iPP} = 3900$; $M_{n,aPS} = 7700$) as the representative. On a vacuum line, tosyl group end-capped iPP ($M_n = 3900$; $M_w/M_n = 1.42$) was dissolved in 50 mL of toluene at 50 °C. The solution was cooled to room temperature and was then charged with excess freshly prepared living anionic aPS ($M_n = 7700$; $M_w/M_n = 1.04$). The resulting solution was slowly warmed to 50 °C and was then maintained at 50 °C for 24 h. The polymer solution was then quenched with excess methanol (ca. 20 mL), and this led to the deposition of the polymer mixture as a white precipitate. The resulting polymer mixture (containing iPP-*b*-aPS, the excess aPS, and the residual tosyl group end-capped

Table 1. Molecular Characteristics of the iPP Homopolymer and the iPP-*b*-aPS Diblock Copolymers Used in the Present Study

block copolymers	M_n (g/mol) ^a (iPP)	PDI ^b (iPP)	M_n (g/mol) ^b (aPS)	PDI ^b (aPS)	M_n (g/mol) (block)	PDI ^b (block)	f^a (iPP)
iPP homopolymer	4300	1.37					1.00
iPP ₄₃ aPS ₅₇ ^{10.4}	4500	1.32	5900	1.02	10400	1.24	0.45
iPP ₃₄ aPS ₆₆ ^{11.6}	3900	1.42	7700	1.04	11600	1.23	0.36
iPP ₂₃ aPS ₇₇ ^{17.8}	4100	1.35	13700	1.04	17800	1.16	0.24

^a M_n (number-average molecular weight) and f (volume fraction) were determined by ¹H NMR spectroscopy (solvent, CDCl₃; temperature, 60 °C).

^b M_n , M_w (weight-average molecular weight), and PDI (polydispersity, M_w/M_n) were determined by high-temperature GPC (solvent, 1,2,4-trichlorobenzene; temperature, 135 °C).

iPP) was isolated after filtration. The purification of the iPP-*b*-aPS was completed in two steps. First, the excess aPS (soluble in boiling acetone) was removed by Soxhlet extraction in boiling acetone. The resulting acetone-insoluble fraction was collected, dried, and allowed to undergo a second Soxhlet extraction with heptane to remove the residual tosyl group end-capped iPP. The resulting heptane-insoluble fraction was collected and dried under vacuum overnight to yield the pure iPP-*b*-aPS as a white solid.

2.1.3. Polymer Analysis. Figure S1 of the Supporting Information shows the ¹H NMR spectrum of the resulting iPP-*b*-aPS ($M_{n,iPP}$ = 3900; $M_{n,aPS}$ = 7700). The spectrum was recorded on a Bruker AV-500 NMR spectrometer to determine the molecular of iPP block in the copolymer. The iPP-based sample was dissolved into CDCl₃ as solvent. The recorded temperature was at 60 °C. The result indicated that the iPP-*b*-aPS diblock copolymer was successfully prepared by using the above synthetic methods.

The average molecular weights and PDI (M_w/M_n) were determined by high-temperature gel permeation chromatography (Waters 150-CALAC/GPC) with a refractive index (RI) detector and a set of U-Styrigel HT columns of 106, 105, 104, and 103 pore sizes in series. The measurements were conducted at 135 °C using 1,2,4-trichlorobenzene as the solvent. PS samples with narrow PDI were used as the standards for calibration. The successful preparation of a structurally well-defined iPP-*b*-aPS ($M_{n,iPP}$ = 3900, $M_{n,aPS}$ = 7700) sample can be further elucidated by the GPC analysis shown in Figure S2 (in the Supporting Information), which compares the GPC elution curves of the tosyl group end-capped iPP (M_n = 3900; M_w/M_n = 1.42) and the living anionic aPS (M_n = 7700; M_w/M_n = 1.04) with that of the iPP-*b*-aPS (M_n = 11 600 g/mol; M_w/M_n = 1.23).

Detailed molecular characteristics of the iPP homopolymer and iPP-*b*-aPS diblock copolymers used in the present study are shown in Table 1. The samples are denoted as iPP_{*x*}aPS_{*y*}^{*M*}, where the subscripts *x* and *y* indicate the composition in wt % of iPP and aPS, respectively, and the superscript *M* signifies the overall number-average molecular weight of the diblock in kg/mol.

2.2. Bulk Sample Preparation. The thick films of iPP homopolymer and iPP-*b*-aPS were prepared by dissolving the polymer powders in toluene at 65 °C. The concentration of the polymers in the solution was 5 wt %. The samples were subsequently cast onto the Petri dish, and the solvent was evaporated slowly at 70 °C. The resultant films were further dried in vacuum at 70 °C for 2 days to completely remove the residual solvent.

2.3. Differential Scanning Calorimetry (DSC) Measurement. DSC experiments were carried out by a TA DSC-2010 instrument to study the crystallization and melting behavior of the diblock copolymer. Samples of ca. 5 mg were encapsulated

in aluminum pans. The calibration was performed with indium and hexatricontan, and all tests were conducted using ultrapure nitrogen as purge gas. In the standard DSC experiments, the samples were first heated to 170 °C (a temperature of ca. 40 °C higher than T_m^{iPP} (the melting point of iPP blocks)) and kept at that temperature for 10 min to erase thermal history. Then, a cooling scan at 10 °C/min was conducted down to −30 °C, followed by a subsequent heating run performed also at 10 °C/min.

2.4. Self-Nucleation Studies. The self-nucleation technique was employed in order to study the effect of self-nuclei on the crystallization behavior of iPP blocks in both homopolymer and diblock copolymer. Detailed experimental procedure can be found in previous works.^{5,38} Briefly, the samples were first heated to 170 °C (which was high enough to completely melt the polymer in order to erase crystalline thermal history) followed by cooling at 10 °C/min down to −30 °C to provide them with a standard thermal history. The samples were then heated again to a so-called self-nucleation temperature (T_s) for isothermal annealing for 30 min. After the treatment at T_s , the DSC scans were conducted by cooling to −30 at 10 °C/min followed by heating at 10 °C/min to 190 °C.

2.5. Time-Resolved Simultaneous SAXS/WAXS Measurements. Simultaneous SAXS/WAXS experiments were performed at Beamline 23A1 at the National Synchrotron Radiation Research Center (NSRRC) located at Hsin-Chu, Taiwan.³⁹ A two-dimensional Mar CCD detector with 512 × 512 pixel resolution was used to record the SAXS pattern. The energy of the X-ray source and the sample-to-detector distance were 10 keV and 2444 mm, respectively. The time necessary for each data collection was 30s. The SAXS intensities obtained were plotted against q ($= 4\pi \sin \theta/\lambda$, where λ is the wavelength of X-ray (λ = 0.124 nm) and 2θ is the scattering angle). The beam center was calibrated using silver behenate with the primary reflection peak at 1.076 nm^{−1}. The WAXS profiles were simultaneously collected with the SAXS profiles using a linear detector, covering the scattering vector range of 8–17.5 nm^{−1}. The WAXS angular scale was calibrated using silicon, sodalite, and high-density polyethylene.

2.6. Transmission Electron Microscopy (TEM) Experiment. The melt morphology of iPP-*b*-aPS was examined by a JEOL JEM-2000FXZ TEM operated at 100 kV. The copolymer specimens were first annealed at 170 °C (higher than T_m^{iPP}) for 10 min, followed by quenching to liquid nitrogen to fix the melt morphology. The copolymer specimens were microtomed at −60 °C with a Reichert Ultracut E low-temperature sectioning system. The microtomed sections were collected onto copper grids coated with carbon-supporting films and then stained by RuO₄(aq) vapor for 15 min. Since RuO₄ was a preferential staining agent for aPS block, aPS and iPP domains appeared as dark and bright regions in the micrographs, respectively.

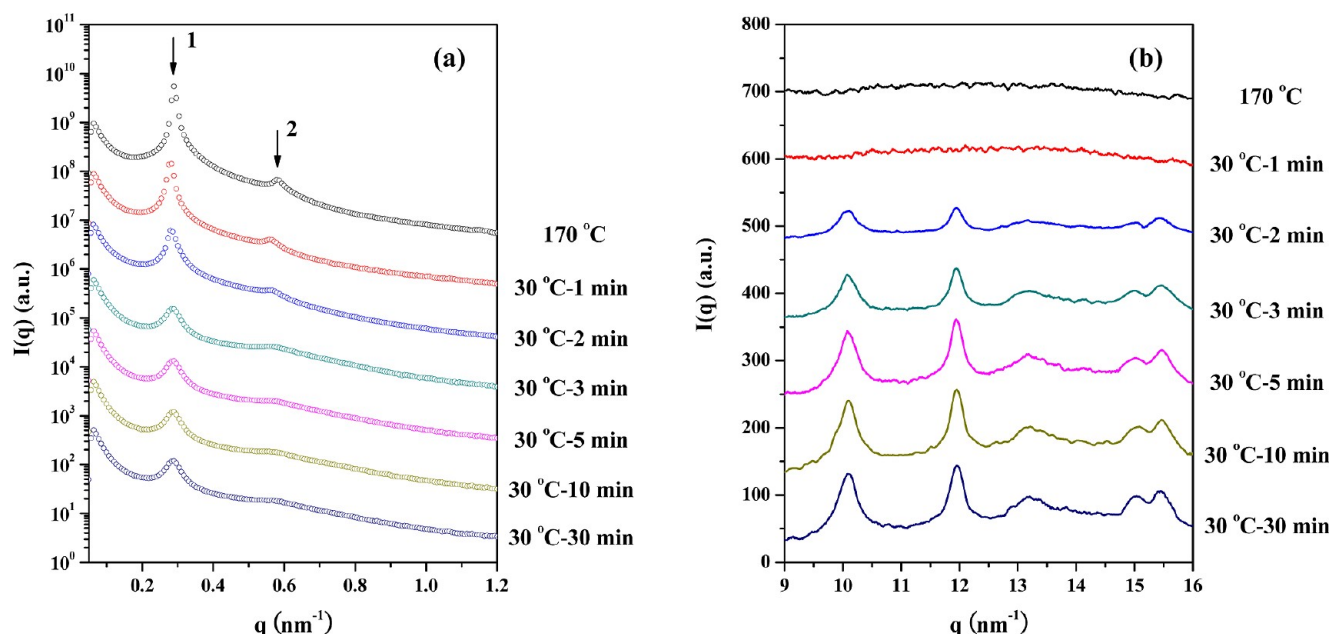


Figure 1. Simultaneous (a) SAXS and (b) WAXS profiles of $\text{iPP}_{43}\text{aPS}_{57}^{10.4}$ collected at 170 °C and, subsequently, at 30 °C at different time.

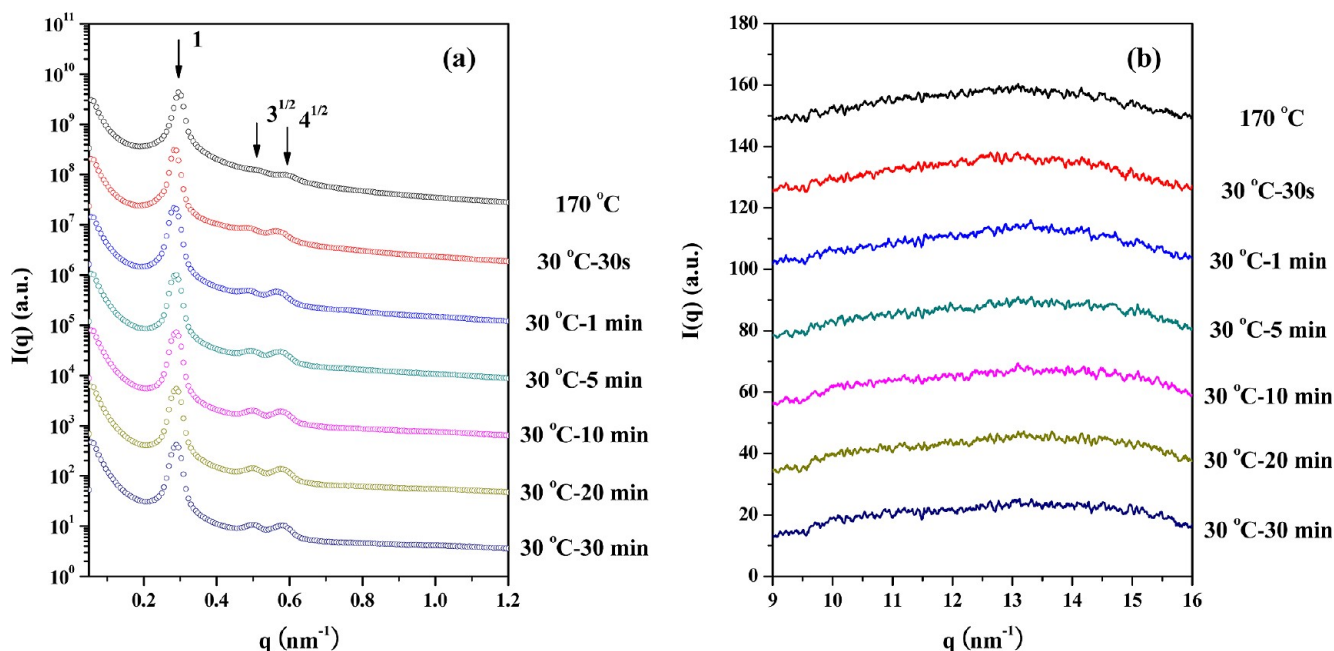


Figure 2. Simultaneous (a) SAXS and (b) WAXS profiles of $\text{iPP}_{34}\text{aPS}_{66}^{11.6}$ collected at 170 °C and, subsequently, at 30 °C at different time.

2.7. Fourier Transform Infrared (FTIR) Spectroscopy.

IR spectra were recorded with a resolution of 1 cm^{-1} over 32 scans using a Nicolet Avatar 320 FTIR spectrometer under nitrogen atmosphere. The iPP homopolymer and iPP-*b*-aPS were dissolved in toluene at 65 °C followed by dropping onto the KBr pellets. The specimens were then placed on a Linkam HFS 91 hot stage at 70 °C to remove the solvent. After solvent removal, the samples were annealed at 170 °C on the hot stage for 10 min to erase the thermal history and then promptly transferred into the DSC sample chamber, which was pre-equilibrated at 5 °C, to allow iPP crystallization. The accuracy of sample temperature control was ± 0.5 °C. All the samples were kept at 5 °C for a sufficiently long time (>36 h) to allow iPP to crystallize to saturation before FTIR measurement. The

IR spectra of the samples were collected in situ at various temperatures in a heating cycle to characterize the population of helical sequence at different temperatures. The resultant films on the KBr pellet were thin enough to be within the absorbance range where the Beer–Lambert law was obeyed. For the molecular conformation characterization, the sample was equilibrated at each temperature for 5 min prior to data acquisition.

2.8. Large-Amplitude Oscillatory Shear (LAOS) Experiment. Large amplitude oscillatory shear was performed to produce large-scale alignment of the microdomains in iPP-*b*-aPS. The shear was carried out with a Linkam CSS 450 shear hot stage in the oscillatory mode with the shear frequency of 0.25 Hz and the strain amplitude of 70%. The samples with the

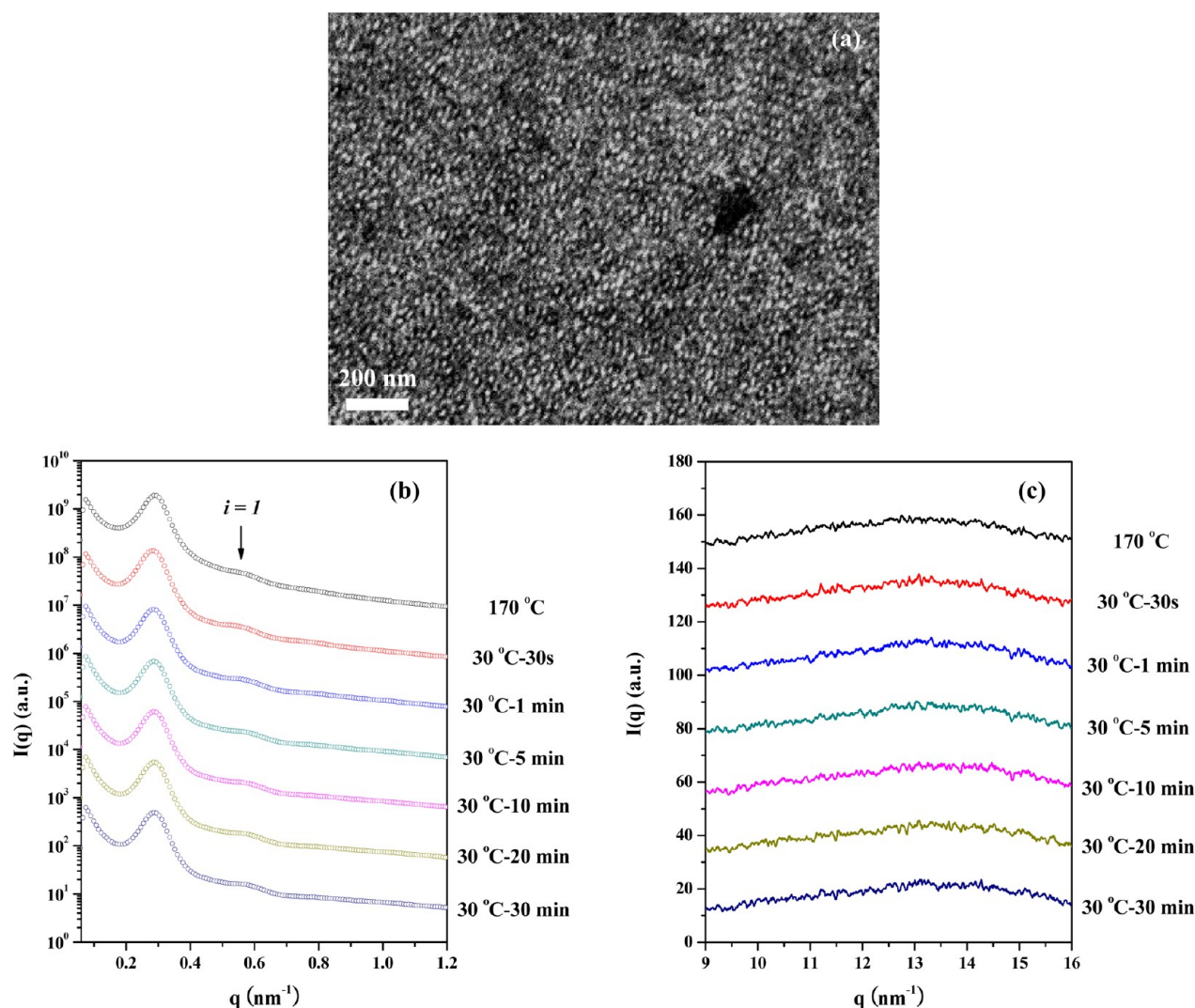


Figure 3. (a) TEM micrograph of $iPP_{23}aPS_{77}^{17.8}$ after quenching from the melt to room temperature. The diblock copolymer was stained with RuO_4 (where the iPP microdomains and the aPS matrix appeared bright and dark, respectively). Simultaneous (b) SAXS and (c) WAXS profiles of $iPP_{23}aPS_{77}^{17.8}$ collected at 170 °C and, subsequently, at 30 °C at different time.

size of $5.0 \times 5.0 \times 0.2 \text{ mm}^3$ were subjected to LAOS for 2 h under a nitrogen atmosphere at 170 °C to achieve good alignment of the lamellar microdomains. The samples after shearing were further treated at the prescribed crystallization temperatures. For $-5 \leq T_c \leq 80 \text{ °C}$, the shear-oriented sample was first annealed at 170 °C on a Linkam HFS 91 hot stage for 10 min to erase the residual stresses and thermal histories. After 10 min, the sample was promptly transferred from the hot stage into the DSC sample chamber, which was pre-equilibrated at the desired T_c . The accuracy of sample temperature control was $\pm 0.5 \text{ °C}$. All the samples were annealed at the T_c for a sufficiently long time ($>48 \text{ h}$) in order to crystallize to saturation before SAXS/WAXD measurement for elucidating the orientation of iPP crystals in the lamellar microdomains.

3. RESULTS AND DISCUSSION

3.1. Microphase-Separated Morphology. Figure 1a,b shows the time-resolved SAXS and WAXS profiles of $iPP_{43}aPS_{57}^{10.4}$, respectively, subjected to the crystallization process at 30 °C. This temperature situated far below the glass transition temperature of aPS block (T_g^{aPS}), and therefore, a hard confinement environment was provided for the

crystallization of iPP blocks. At 170 °C (ca. 40 °C higher than T_m^{iPP}), the SAXS profile displayed a pair of diffraction peaks with the position ratio of 1:2, indicating that $iPP_{43}aPS_{57}^{10.4}$ formed a lamellar morphology with the inter-lamellar distance (L) of 21.9 nm in the melt state. Upon quenching to 30 °C, the iPP blocks started to crystallize at 2 min and the crystallinity reached saturation after 5 min, as evidenced by the WAXS profiles (see Figure 1b, where the peaks observed at 10.1, 11.9, 13.2, 15.0, and 15.4 nm^{-1} are associated with the (110), (040), (130), (111), and (131)/(041) diffractions of the α -form iPP crystal, respectively). The fact that the position of the primary SAXS peak did not change apparently (Figure 1a) indicated that the lamellar morphology established in the melt remained essentially unperturbed upon iPP crystallization since the crystallization was effectively confined within the microdomains surrounded by the glassy aPS domains. However, the SAXS intensity decreased significantly upon iPP crystallization due to the reduction of the electron density contrast between iPP and aPS domain. The SAXS/WAXS results hence indicate that the crystallization of iPP block was strictly confined within the lamellar microdomains established by the melt mesophase.

In the case of $iPP_{34}aPS_{66}^{11.6}$, the SAXS profile at 170 °C (Figure 2a) showed multiple scattering peaks with the position ratio of $1:3^{1/2}:4^{1/2}$, indicating that the copolymer exhibited the hexagonally packed cylinder morphology, where the minority iPP blocks formed the cylindrical microdomains dispersed in the aPS matrix. The interdomain distance (D) calculated from the primary peak position was 24.6 nm, and the average radius (R) of the iPP cylinders was 7.7 nm as derived from its volume fraction in the melt state ($f_{iPP} = 0.36$). The melt morphology was also confirmed by the TEM micrograph (see Figure S3 in Supporting Information), where a clear hexagonal array of iPP cylinders (with the radius of the cylindrical microdomains of ca. 7.3 nm) dispersed in the aPS matrix was observed.

Figure 2a,b shows the time-resolved SAXS and WAXS profiles of the cylinder-forming $iPP_{34}aPS_{66}^{11.6}$, respectively, subjected to the same thermal history as that employed for $iPP_{43}aPS_{57}^{10.4}$. When the temperature was lowered to 30 °C, the intensity of the SAXS peaks enhanced slightly due to the increase of segregation strength, while the initial morphology established by the microphase separation was preserved. Unlike $iPP_{43}aPS_{57}^{10.4}$, the iPP block in $iPP_{34}aPS_{66}^{11.6}$ was virtually uncrystallizable at 30 °C in 30 min, as manifested by the WAXS profiles in Figure 2b. This was attributed to the change of the required nucleation mechanism from heterogeneous (in lamellae-forming $iPP_{43}aPS_{57}^{10.4}$) to homogeneous nucleation (in cylinder-forming $iPP_{34}aPS_{66}^{11.6}$), where the initiation of crystallization in the highly isolated cylindrical microdomains needs to proceed through homogeneous nucleation, which requires exceedingly large undercooling.

A disordered sphere morphology was observed in the TEM micrograph of $iPP_{23}aPS_{77}^{17.8}$ (see Figure 3a), where iPP nanospheres dispersed in the aPS matrix did not exhibit apparent long-range order. Figure 3b,c displays the time-resolved SAXS and WAXS profiles of this diblock copolymer, respectively. A SAXS peak (at 0.29 nm^{-1}) associated with the microphase separation was observed at 170 °C. iPP block did not crystallize as the temperature was lowered to 30 °C (cf. the WAXS profiles in Figure 3c), due again to the fact that homogeneous nucleation was required for the crystallization. The enhancement of SAXS intensity and the emergence of a form factor peak (marked by $i = 1$) at 30 °C was attributed to the increase of segregation strength. The position of the form factor peak prescribed the radius of the spherical microdomains via $R = 5.765/q_{m=i=1}$ of 10.3 nm.⁴⁰

The melt structures of the three iPP-*b*-aPS diblock copolymers studied here are summarized in Table 2. It is

Table 2. Microphase-Separated Morphology of the iPP-*b*-aPS Diblock Copolymers

block copolymers	observed morphology (examined by SAXS or TEM)	predicted morphology (based on the volume fraction)
$iPP_{43}aPS_{57}^{10.4}$	lamellae	lamellae
$iPP_{34}aPS_{66}^{11.6}$	iPP cylinders	gyroid
$iPP_{23}aPS_{77}^{17.8}$	iPP spheres	iPP cylinders

worth noting that the observed morphology of the two asymmetric diblocks was not in line with that found for conventional diblock copolymers such as polystyrene-*block*-polyisoprene (PS-*b*-PI).⁴¹ The volume fraction of iPP block in $iPP_{34}aPS_{66}^{11.6}$ and $iPP_{23}aPS_{77}^{17.8}$ was 0.36 and 0.24, respectively; therefore, they are anticipated to show gyroid and hexagonally packed cylinder morphology, respectively, according to the

classical phase diagram.^{3,42} However, the morphologies observed here were hexagonally packed cylinders and disordered spheres, respectively. Considering that the polydispersity indices (PDI) of iPP blocks in these diblock copolymers were quite high before coupling with the aPS block (e.g., 1.42 for $iPP_{34}aPS_{66}^{11.6}$ and 1.35 for $iPP_{23}aPS_{77}^{17.8}$, see Table 1), such a deviation may be attributed to the polydispersity effect.⁴³ Several studies have examined the influence of PDI on the microphase separation behavior of diblock copolymer systems. It was found that the increase of PDI in the minority block (i.e., iPP block in present system) would cause a change of microdomain to the one with larger mean interfacial curvature. Therefore, the gyroid may change to cylinder, and the cylinder may alter to sphere. In this case, the diblock copolymer (with high PDI for the minority block but low PDI for the majority component) can be considered as a mixture of diblock molecules of different lengths of the minority block. Such a blend would exhibit the so-called cosurfactant effect, which tends to shift the phase boundary and decouple the effect of composition on the morphology of the diblock copolymer system.^{44,45} The unexpected morphology observed for $iPP_{34}aPS_{66}^{11.6}$ and $iPP_{23}aPS_{77}^{17.8}$ may thus be explained by this cosurfactant argument.

3.2. Crystallization Behavior. The crystallization kinetics and the melting behavior of the diblocks were assessed by DSC. The crystallization kinetics of iPP blocks within different types of microdomain can be evaluated by the DSC cooling scans under a given cooling rate (10 °C/min). Here, the sample was first annealed at 170 °C ($>T_m^{iPP}$) for 10 min followed by cooling at 10 °C/min to record the crystallization exotherm. The peak temperature of the exotherm is defined as the freezing temperature (T_f), where a higher T_f corresponds to a faster crystallization rate. Figure 4a,b shows the DSC cooling scans, and the subsequent heating scans of iPP homopolymer and the three iPP-*b*-aPS copolymers, respectively. iPP homopolymer exhibited a T_f and a melting temperature (T_m) of 97.7 and 126.7 °C. T_f of the iPP blocks in the lamellae-forming $iPP_{43}aPS_{57}^{10.4}$ was 90.9 °C, which was slightly lower as compared with that of the iPP homopolymer with similar molecular weight. The slight depression of crystallization rate was attributed to the restriction in chain motion of iPP block by pinning the junction points to the interface.

T_f dropped considerably by as much as 74 °C in $iPP_{34}aPS_{66}^{11.6}$ (with $f_{iPP} = 0.36$), when the microdomain morphology of iPP transformed into cylinders. When the volume fraction of iPP was decreased further to 0.26 (i.e., for $iPP_{23}aPS_{77}^{17.8}$), T_f dropped by another 8 °C as the iPP domains transformed to spheres. From the DSC result, we have identified a distinct correlation between microdomain morphology and crystallization kinetics for the iPP-*b*-aPS system. This feature is consistent with that previously found for the blend system of PEO-*block*-poly(1,4-butadiene) (PEO-*b*-PB) and PB by Chen et al.,^{13,14} suggesting that the crystallization rate was predominantly controlled by homogeneous nucleation when microdomain morphology transformed to cylinders or spheres.

The homogeneous nucleation occurred within iPP droplets dispersed in aPS matrix has been studied by Arnal et al.^{46,47} The addition of a sufficient amount of compatibilizer to iPP/aPS blends produced iPP droplets of small size (ca. 1.5 μm in diameter). Homogeneous nucleation of iPP within the droplets was found to take place at a low temperature of 46 °C (corresponding to the undercooling, $\Delta T = T_m - T_b$ of ca. 110 K). This undercooling was comparable to that found for

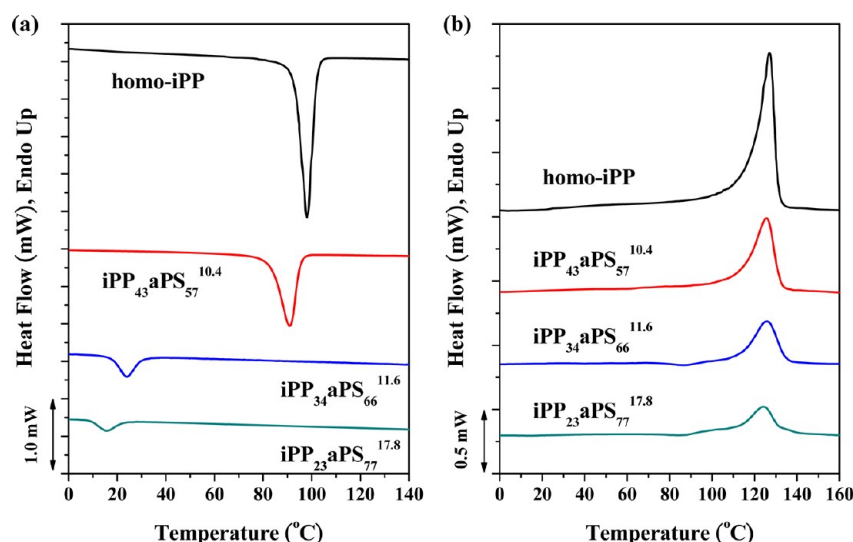


Figure 4. (a) DSC cooling scans (at 10 °C/min) from the melt and (b) the subsequent heating scans (at 10 °C/min) of iPP homopolymer and iPP-*b*-aPS.

iPP₃₄aPS₆₆^{11.6} and iPP₂₃aPS₇₇^{17.8} (where $\Delta T = 102$ and 108 K for iPP₃₄aPS₆₆^{11.6} and iPP₂₃aPS₇₇^{17.8}, respectively) and thus confirmed that homogeneous nucleation of iPP blocks had to occur to induce the crystallization in these two compositions.

3.3. Self-Nucleation Study. For iPP-*b*-aPS, the crystallization in the iPP lamellar microdomains should proceed via heterogeneous nucleation followed by long-range crystal growth because the crystallization can be initiated at the normal undercooling (i.e., the undercooling was comparable to that of iPP homopolymer). On the contrary, the very large undercooling required for crystallization in cylindrical and spherical microdomains implied not only the homogeneous nucleation mechanism but also highly frustrated crystal growth. Here, we employed a self-nucleation (SN) experiment to distinguish the effect of produced self-nuclei on the crystallization behavior in these microphase-separated structures. For this experiment, the sample was first heated to 170 °C, which was high enough to completely melt the crystals in order to erase the previous crystallization history, followed by cooling to -30 at 10 °C/min to provide a standard crystallization history (such a cooling process is denoted as standard cooling). The sample was then heated to a temperature T_s (which is called self-nucleation temperature) and kept there for 30 min. After the annealing at T_s , the sample was cooled to -30 °C and, subsequently, heated to 190 °C (a temperature higher than the end of melting peak) at 10 °C/min. Depending on T_s , the behavior of the crystallization occurred upon cooling to -30 °C can be classified into three domains:^{5,38} (1) Domain I, the sample is completely molten at T_s ; (2) Domain II, the sample is self-nucleated; although T_s is high enough to melt almost all crystals, the self-seeds arising from crystal fragments or crystallization precursors still exist, such that the nucleation density in the subsequent crystallization increases enormously; (3) Domain III, the sample is partially molten, such that the self-nucleation and annealing of unmelted crystals take place at T_s . The influence of the microdomain morphology on the SN behavior of iPP crystallization will be discussed as follows.

For iPP block crystallized within the lamellar microdomains (i.e., iPP₄₃aPS₅₇^{10.4}), Figure 5a,b shows the cooling and subsequent heating traces obtained after SN treatments at T_s .

For $T_s \geq 130$ °C, no change in freezing temperature with T_s was found, and the observed T_f was comparable to that found in the standard cooling trace; therefore, this T_s range corresponded to Domain I. At $T_s = 129$ °C, T_f in the cooling scan shifted slightly to higher temperature (see Figure 5a), whereas annealing of unmelted crystals at T_s was not detected in the subsequent heating run (Figure 5b). Thus, Domain II started from $T_s = 129$ °C. This domain indeed spanned over the T_s range of 126–129 °C, where the crystallization rate was found to accelerate with decreasing T_s in this regime. At $T_s = 124$ °C, the system started to exhibit the annealing of unmelted crystals, as can be seen from the appearance of a melting peak at 134.6 °C in the corresponding heating scan (Figure 5b). This effect became more pronounced upon lowering T_s to 120 °C (where the iPP blocks crystallized immediately upon cooling from this temperature), revealing an increase of peak area of the higher-temperature endotherm. Consequently, the system approached Domain III at $T_s = 124$ °C. In Domain III, since a portion of crystals remained unmelted, they served as the nuclei from which crystal growth started preferentially. On the basis of the fact that the crystal growth can advance over a long-range in lamellae-forming diblock, the presence of these residual nuclei would significantly promote the overall crystallization rate. Therefore, the samples treated by SN procedure in this temperature regime (Domain III) would crystallize faster than those treated at T_s located in Domain I. The SN domains for the iPP block in lamellae-forming iPP₄₃aPS₅₇^{10.4} can be depicted in Figure 5c. The crystallization of iPP within the lamellar microdomains obeyed the classical SN behavior as that displayed by the homopolymer (in the sense that all three SN domains have been observed).

We now turn our attention to iPP blocks crystallized within the isolated cylindrical microdomains (formed in iPP₃₄aPS₆₆^{11.6}). Figure 6a,b shows the cooling and subsequent heating traces after performing the SN treatments at the indicated T_s . For $T_s \geq 129$ °C, no change in crystallization peak was observed (as compared with the standard cooling scan in Figure 6a), this T_s range hence corresponded to Domain I. At $T_s = 128$ °C, although the crystallization peak did not shift in comparison with the standard cooling trace, the subsequent heating run exhibited an additional higher-temperature melting

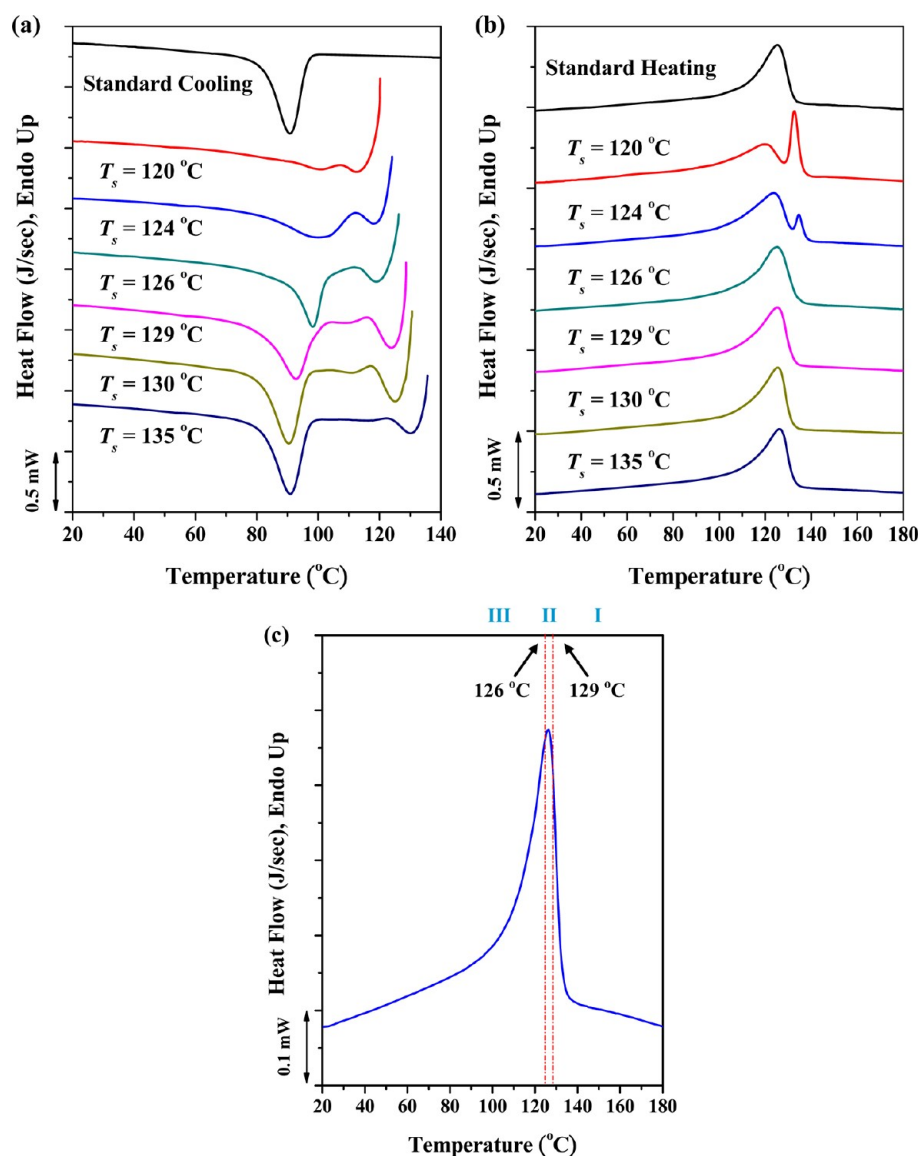


Figure 5. (a) DSC cooling scans at 10 °C/min after self-nucleation of $iPP_{43}aPS_{57}^{10.4}$ at the indicated self-nucleation temperatures (T_s); (b) subsequent heating scans at 10 °C/min; and (c) self-nucleation domains for the iPP block in $iPP_{43}aPS_{57}^{10.4}$.

peak (as revealed in Figure 6b). Therefore, Domain III has been reached at $T_s \leq 128$ °C, where the annealing of unmelted crystals occurred. A further decrease in T_s resulted in an increasing amount of annealed iPP crystals. This in turn caused a great amount of annealed crystals as evidenced by the increase in the peak area of the higher-melting endotherm (Figure 6b). It is, however, interesting to note that the crystallization exotherm unexpectedly moved to lower temperature (indicating a decrease of crystallization rate) when T_s was lower than 128 °C (Figure 6a). This can be attributed to the fact that the crystal growth was highly frustrated as the crystallization was largely confined within the cylindrical microdomains; therefore, the residual nuclei remained in a small portion of microdomains would not assist the crystallization in the others. In this case, most microdomains still had to acquire new nuclei to initiate their own crystallizations. Because crystals already existed in a portion of microdomains, the probability of inducing the homogeneous nucleation in the remaining molten domains was reduced, so that decreasing T_s in Domain III would exert a retardation effect on the kinetics of the subsequent

crystallization (instead of the acceleration effect appeared in the general case of Domain III found for the crystallization in homopolymers and lamellae-forming diblock). The observed SN domains of $iPP_{34}aPS_{66}^{11.6}$ are presented on the standard melting peak in Figure 6c. It can be seen that Domain II was completely absent in $iPP_{34}aPS_{66}^{11.6}$. This anomalous behavior seemed to be an intrinsic property for the crystallizable block when it was effectively confined within the isolated microdomains⁴⁸ as compared to the conventional SN behavior appearing in the crystallizable homopolymer or lamellae-forming C-A diblock copolymers. The absence of Domain II in the isolated microdomains was ascribed to the unique nucleation mechanism (i.e., homogeneous nucleation) and the highly frustrated crystal growth of the crystallizable block.

Figure S4a,b, Supporting Information, shows the crystallization and melting behavior of $iPP_{23}aPS_{77}^{17.8}$ after subjecting to the SN treatment at the indicated T_s , respectively, where the iPP block was now confined within the spherical microdomains. The SN domains are presented in Figure S4c, Supporting Information. The characteristic of the SN behavior found in this

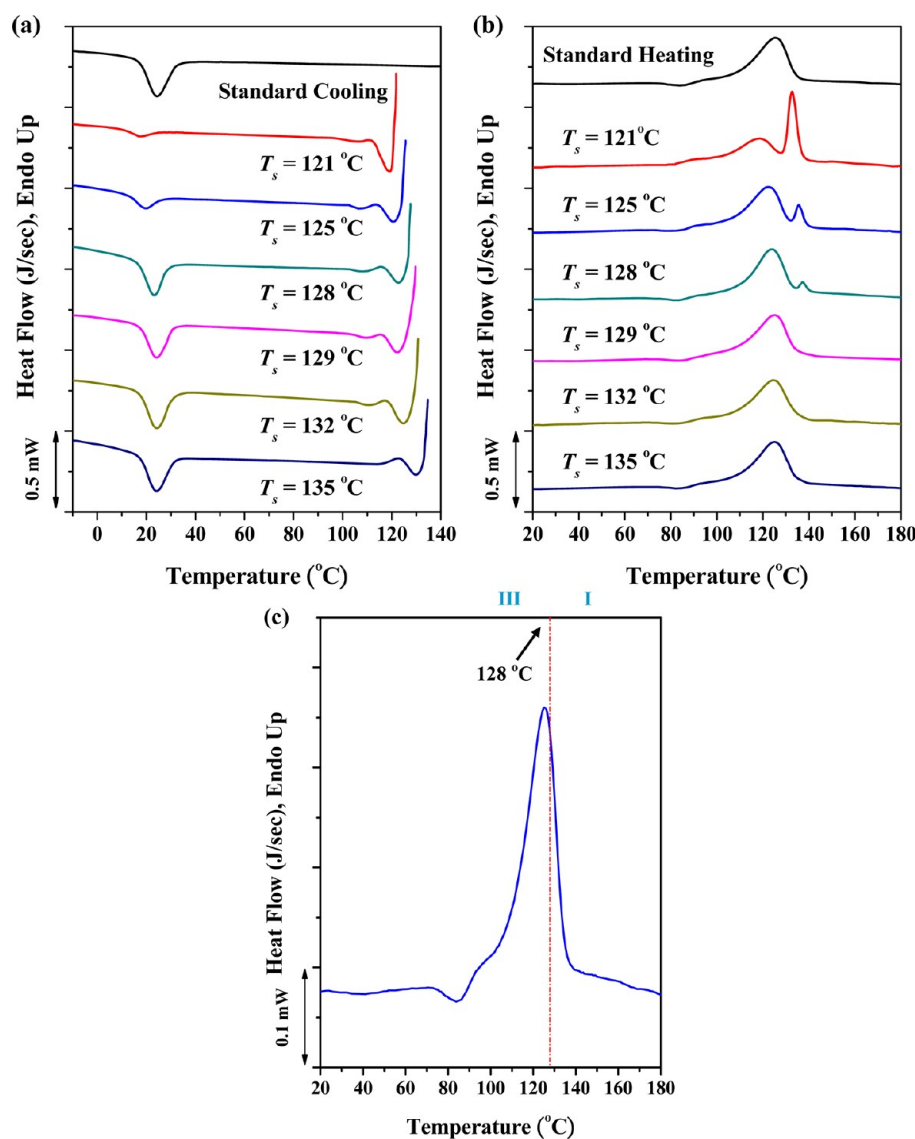


Figure 6. (a) DSC cooling scans at 10 °C/min after self-nucleation of iPP₃₄aPS₆₆^{11,6} at the indicated self-nucleation temperatures (T_s); (b) subsequent heating scans at 10 °C/min; and (c) self-nucleation domains for the iPP block in iPP₃₄aPS₆₆^{11,6}.

sample was similar to that observed in iPP₃₄aPS₆₆^{11,6} since the crystallization of iPP block was strictly confined within the isolated microdomains. Hence, a direct transition from Domain I to Domain III occurred at 127 °C without passing through Domain II. On the basis of the systematic analysis of the SN results, the correlation among the confinement geometry, the nucleation mechanism, and the length scales of crystal growth has been established.

3.4. Population of Helical Sequence of iPP Block in Different Microdomains. It is known that the microphase separation in block copolymers would induce the minority blocks to stretch normal to the interface, and the degree of stretching increases with increasing interfacial curvature (i.e., sphere > cylinder > lamellae). Since we have demonstrated that the iPP-*b*-aPS under study can construct three types of confinement geometries for iPP blocks (while keeping the molecular weight of iPP similar), it is of interest to understand if the intrinsic chain stretching mediated by the microdomain structure would affect the stability of the longer helical sequence in the iPP block in the melt state. To study this issue, we examined the absorbances of the helical bands in the

IR spectra as a function of temperature upon stepwise heating to evaluate the population of helical sequence at various temperatures.

The lengths of the helical sequence associated with various helical bands have been well established for iPP. The bands at 940, 1220, 1167, 1303, 1330, 841, 998, 900, 808, 1100, and 973 cm⁻¹ were identified as the helical bands of iPP.^{18–21} The minimum values of monomers (n) in the helical sequences for the appearance of the bands at 973, 998, 841, and 1220 cm⁻¹ were found to be 5, 10, 12, and 14, respectively.^{20,21} It is noted that the helical bands may still persist above the melting point of iPP as they are related to the intramolecular (instead of intermolecular) coupling. Figure 7a shows the IR spectra collected at different temperatures for iPP homopolymer. During the heating process, the 940 cm⁻¹ band disappeared first at 130 °C, then the bands at 1220, 1167, 1303, 1330, 841, 900, 808, and 1100 cm⁻¹ vanished progressively across 130–135 °C (corresponding to the nominal melting region detected by DSC). Although the 998 cm⁻¹ band (corresponding to $n \geq 10$) still existed at 200 °C, the intensity was considerably weakened. Considering the 973 cm⁻¹ band, it has been

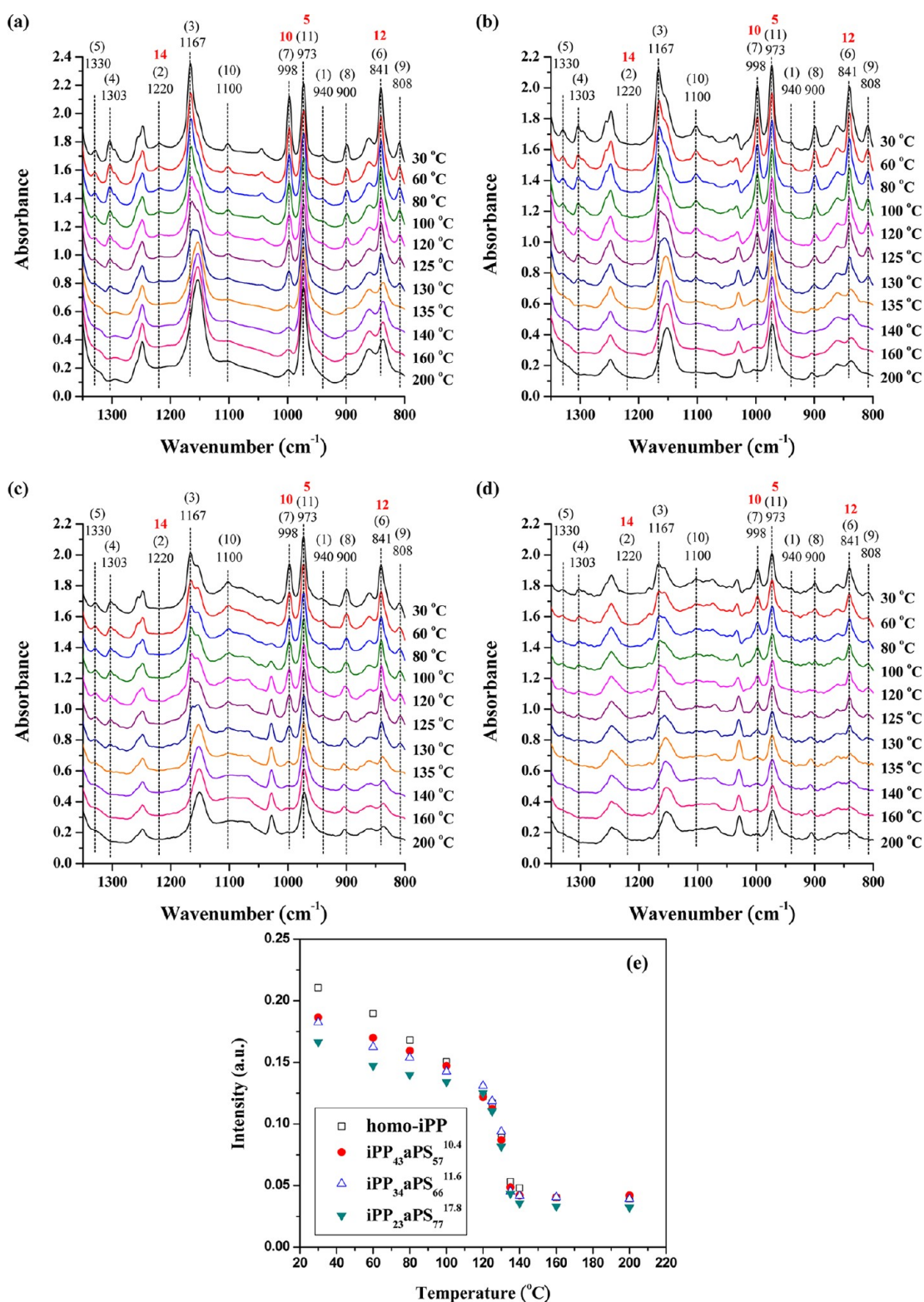


Figure 7. Temperature-dependent IR spectra of (a) iPP homopolymer; (b) $\text{iPP}_{43}\text{aPS}_{57}^{10.4}$; (c) $\text{iPP}_{34}\text{aPS}_{66}^{11.6}$; and (d) $\text{iPP}_{23}\text{aPS}_{77}^{17.8}$. The sample was first crystallized to saturation, and then, the FTIR measurement was carried out by stepwise heating. The number in the parentheses corresponds to the degree of order of the iPP 3/1 helical sequence of the indicated bands. The number marked by red signals the minimum value of monomers (n) for the appearance of the indicated helical bands. (e) The reduction of the population of helical sequence represented by ratio of the area of the 998 cm^{-1} band to that of the 1460 cm^{-1} band with increasing temperature.

reported that this band was not only contributed by the head-to-tail sequence of the repeating units but also associated with the presence of short iPP helices.⁴⁹ The dependence of the helical band intensity on the temperature upon heating

observed here was in line with the previous study reported for iPP with relatively high molecular weight.^{20,21}

Figure S5, Supporting Information, shows the IR spectra of $\text{iPP}_{43}\text{aPS}_{57}^{10.4}$ collected at 30 °C. In this case, the iPP blocks

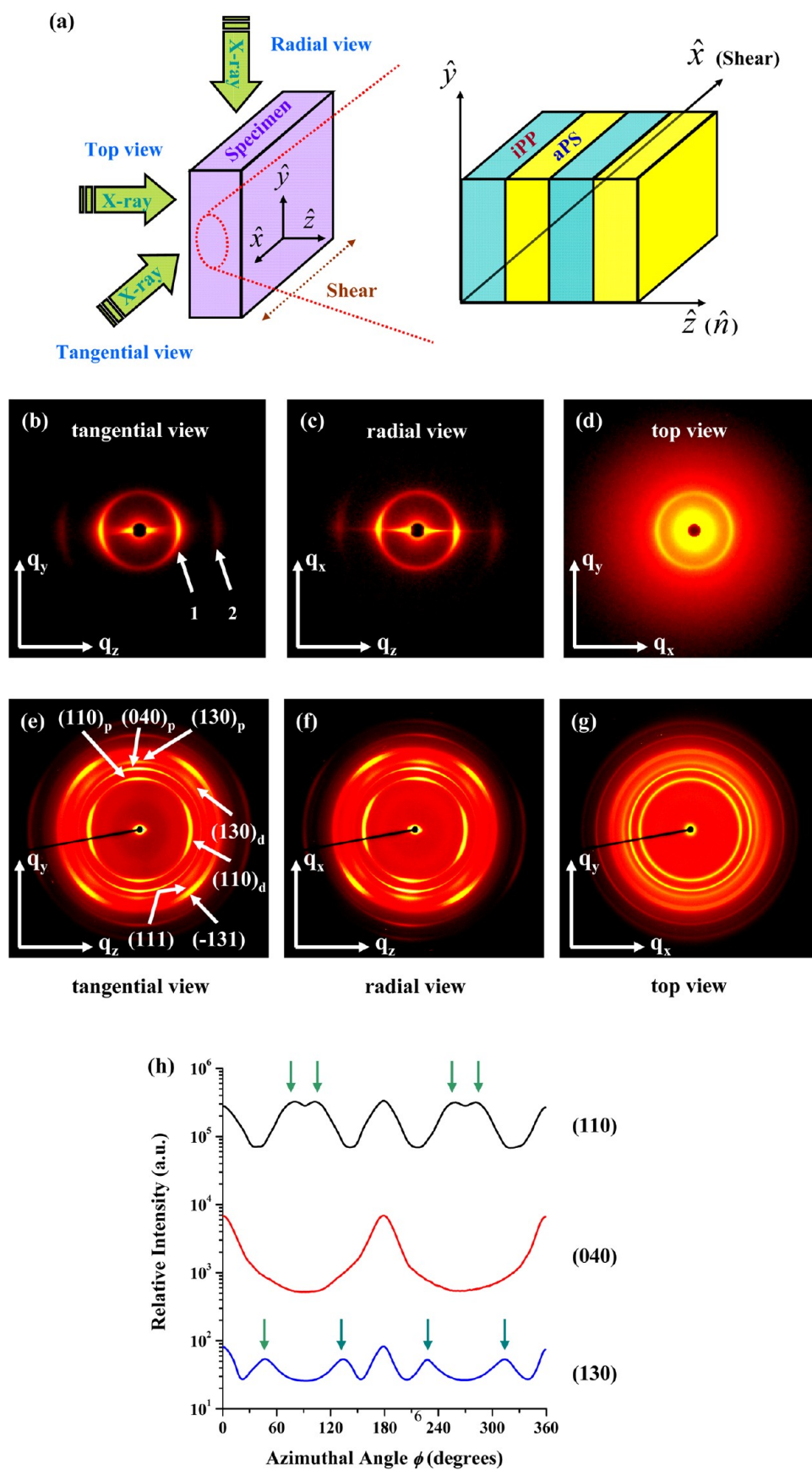


Figure 8. continued

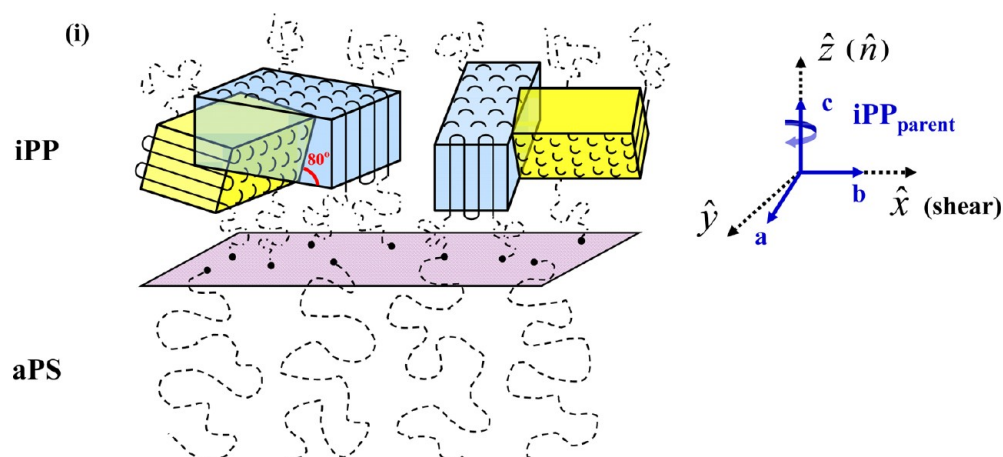


Figure 8. (a) Schematic illustrations of the geometry of the shear-oriented $iPP_{43}aPS_{57}^{10.4}$, indicating different incident directions of the X-ray for obtaining the 2D scattering patterns in tangential-view (the X-ray beam is traveling along \hat{x}), radial-view (the X-ray is along \hat{y}), and top-view (the X-ray is along \hat{z}). The illustration on the right shows the alignment of the lamellar microdomains attained after the shear treatment. (b) Tangential-view, (c) radial-view, and (d) top-view of the 2D SAXS patterns of shear-oriented $iPP_{43}aPS_{57}^{10.4}$ after being isothermally crystallized at 30 °C. (e) Tangential-view, (f) radial-view, and (g) top-view of the 2D WAXD patterns of shear-oriented $iPP_{43}aPS_{57}^{10.4}$ after being isothermally crystallized at 30 °C. The system was cooled from 170 to 30 °C to allow for iPP crystallization. The subscript p and d marked in the (hkl) diffraction planes of the 2D WAXD patterns represent that the appearance of the specific diffraction was attributed to the parent and daughter crystals, respectively. (h) The azimuthal scans of (110), (040), and (130) diffractions of α -form iPP crystals. The intensities of (110) and (130) diffractions marked by arrows were contributed by the daughter lamellae, due to the lamellar branching in the α -form iPP crystals. (i) Schematic presentation of the perpendicular orientation of the parent crystals as well as the development of the daughter lamellae, where the angle between the crystalline stems in parent (marked in cyan) and daughter (marked in yellow) crystals was ca. 80° or 100°.

were confined within the lamellar microdomains. Since the absorption bands of aPS overlapped significantly with the helical bands of iPP (around 940, 1220, 1303, 1330, 841, 998, and 900 cm^{-1}), direct observation of the contribution from iPP helical sequences was difficult. Therefore, a spectral subtraction was applied to obtain the difference spectra contributed mainly by iPP by subtracting the pure aPS spectra from the block copolymer spectra at a given temperature. For the subtraction, the absorption band of aPS at 540.5 cm^{-1} (which was associated with the out-of-plane vibrational modes of C–H of the aromatic ring)⁵⁰ was used as the reference to determine the scaling factor for the subtraction. The difference spectra were obtained as this band was completely eliminated. The temperature-dependent difference spectra of $iPP_{43}aPS_{57}^{10.4}$, $iPP_{34}aPS_{66}^{11.6}$, and $iPP_{23}aPS_{77}^{17.8}$ are shown in Figure 7b–d, respectively. On the basis of the fact that the absorption band at 998 cm^{-1} always preserved at the temperatures above the nominal melting point (see Figure 7a–d), here, we mainly concentrated on this helical band (which is associated with the longer helical sequences comprising at least 10 monomers in each sequence) to investigate the effect of chain stretching in the microdomains on the stability of the longer helices in the melt state. The band at 1460 cm^{-1} was due to the asymmetric deformation vibration of the methyl group, which is insensitive to the helical conformation of iPP,¹⁹ we thus used this band as an internal standard to quantify the amount of helical sequences (represented by the ratio of the area of the 998 cm^{-1} peak to that of the 1460 cm^{-1} band). The temperature dependencies of the intensity ratios are displayed in Figure 7e. It can be seen that the diminishment of the helical bands in the copolymers was quite similar to that exhibited by the iPP homopolymer, where the helical sequence was disrupted significantly across 130–135 °C. The difference in the intensity ratios of the four specimens below 120 °C was ascribed to the different crystallinities of iPP in these samples. However, when the temperature was higher than 140 °C (corresponding to the

end of the melting peak detected by DSC, cf. Figure 4b), the amount of helical sequence was essentially identical for the four samples. This result indicated that the population of the longer helical sequence was mainly affected by temperature but not by the confinement, chain stretching, and junction point constraint associated with the microdomain formation. IR spectroscopy probes the local conformational structure at the length scale of several monomer units of the polymer chain; the fact that such a local structure was unperturbed when the chains were confined in the microdomains indicated that the stretching of the block chains occurs at a global length scale. This is consistent with the picture of stretching a polymer chain by tension, where the chain can be visualized to comprise a sequence of blobs.⁵¹ On the length scale smaller than the blob size, the conformation remains essentially unperturbed, while on length scales larger than the blob, the cumulative stretching energy is larger than $k_B T$, and the chain gets stretched.

3.5. Orientation of α -Form iPP Crystals in the Lamellar Microdomains. In order to reveal the crystal orientation in the lamellae-forming $iPP_{43}aPS_{57}^{10.4}$, the copolymer was first subjected to the large-amplitude oscillatory shear (LAOS) at 170 °C (which is ca. 40 °C higher than the T_m^{iPP}) for 2 h to produce a large-scale alignment of the microdomains in the sample. The sheared diblock was then cooled to the desired T_c (ranging from –5 to 80 °C) to allow iPP crystallization. Over the T_c range investigated, only the α -form iPP crystals formed. The α -form crystals were found to coexist with the γ -form when T_c was higher than 90 °C, but this scenario was not considered here. Two-dimensional SAXS and WAXD patterns of the crystalline sample were obtained to resolve the orientation of iPP crystals with respect to the lamellar interface. The geometry of the specimen after shearing is schematically illustrated in Figure 8a. The shear direction is denoted as \hat{x} , and the gradient direction is along \hat{z} . It will be shown that the lamellar normal (\hat{n}) is along \hat{z} . The tangential-, radial-, and top-view SAXS/WAXD patterns of the films were collected by

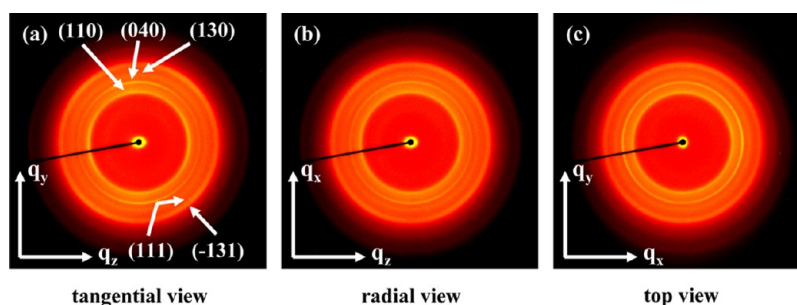


Figure 9. (a) Tangential-view, (b) radial-view, and (c) top-view of the 2D WAXD patterns of shear-oriented $\text{iPP}_{43}\text{aPS}_{57}^{10,4}$ after isothermal crystallization at 10 °C. The system was quenched from 170 to 10 °C to allow for iPP crystallization.

having the incident X-ray traveling along \hat{x} , \hat{y} , and \hat{z} , respectively (see Figure 8a).

Figure 8b–d shows the representative 2D SAXS patterns of the sample having been crystallized at 30 °C. The scattering patterns obtained from tangential (Figure 8b) and radial view (Figure 8c) were practically identical, showing a pair of reflections at the equator with the position ratio of 1:2, which indicated the presence of lamellar morphology with the interlamellar distance of 22.7 nm. The scattering patterns and the value of interlamellar distance were essentially identical to those found in the melt state (cf. Figure 1a), signaling that the melt morphology was effectively preserved upon iPP crystallization. The lamellar domains in the sheared sample were thus deduced to be macroscopically aligned with the lamellar normal directed along \hat{z} (i.e., the gradient direction). Similar SAXS patterns were observed for other T_c s (ranging from –5 to 80 °C).

Figure 8e–g displays the corresponding 2D WAXD patterns of $\text{iPP}_{43}\text{aPS}_{57}^{10,4}$ having been crystallized at 30 °C. The diffraction patterns of the samples crystallized at $15 \leq T_c \leq 80$ °C were indeed similar. The anisotropic diffraction patterns associated with iPP crystals obtained from the tangential (along \hat{x}) and radial (along \hat{y}) views were essentially identical, whereas that obtained from the top view (along \hat{z}) showed isotropic rings. This means that iPP crystal orientation in the lamellar microdomains was identical when viewed along the \hat{x} and \hat{y} directions, but the orientation was random when viewed along \hat{z} . In tangential- and radial-view patterns, three strong meridian diffractions observed at 10.1, 11.9, and 13.2 nm^{–1} were associated with the (110), (040), and (130) diffractions of the α -form iPP crystals (with the monoclinic unit cell), respectively.⁵² The ($hk0$) diffractions were found to locate at the meridian in both tangential- and radial-view patterns, but they showed isotropic rings in the top-view pattern, which indicated that the crystalline stems of iPP crystals were preferentially aligned parallel to the lamellar normal (while the a and b axes arranged randomly). That is, the iPP crystals adopted perpendicular orientation over the T_c range of $15 \leq T_c \leq 80$ °C.

However, if all the iPP crystals exhibited perpendicular orientation in the lamellar microdomains, the (110) and (130) diffractions should not appear at the equator and the quadrant, respectively (cf. Figure 8e,f). This fact can be revealed more clearly from the azimuthal scans (obtained by scanning the intensity of a specific diffraction around the azimuthal angle (ϕ) starting from the vertical direction of the pattern) shown in Figure 8h, where the (110) and (130) diffractions located at other than the meridian were indicated by the arrows. The additional strong (110) diffraction (situating near the equator,

i.e., at $\phi = 78.7, 102.5, 258.5$, and 282.7° in Figure 8h) and the (130) diffraction (at four quadrants, i.e., at $\phi = 47.2, 132.8, 226.3$, and 312.8° in Figure 8h) were attributed to the lamellar branching in the α -form iPP crystals.^{17,53} Lamellar branching is a unique property of α -form iPP, where the branches exhibit a distinct orientation with respect to the original crystalline lamellae. This is also termed the parent–daughter relationship. The molecular mechanism of lamellar branching was ascribed to the epitaxy of the daughter lamellae on the lateral (010) faces of the parent lamellae.⁵³ The epitaxy was favored by the approximate identity of a - and c -axis dimensions of the α monoclinic unit cell of iPP, which resulted in a mistake in the sequence of layers of right- and left-handed helices in successive (010) crystallographic planes. Once the mistake occurred, the crystalline stems (c -axis) from the daughter lamellae deposited on the a -axis of the original parent crystals, leading to an angle of 80° or 100° between the crystalline stems in parent and daughter crystals to attain the lattice matches. On the basis of this fact, the lamellar branching is schematically illustrated in Figure 8i. The parent crystals exhibiting perpendicular orientation (with the iPP crystalline stems aligning perpendicular to the interface of the lamellar microdomains) gave rise to the (110) and (130) diffractions at the meridian in both tangential- and radial-view WAXD patterns (cf. Figure 8e,f), whereas these diffractions situating at other directions (cf. the azimuthal angles marked by arrows in Figure 8h) were associated with the daughter lamellae. The perpendicular orientation of iPP crystals (i.e., the parent lamellae) was hence identified for the first time for the iPP-based C-A diblocks, and this type of orientation has frequently been observed among C-A diblock copolymers.^{6,22–25,30–32} Different from other C-A systems, the lamellar branching occurred when the crystallization of iPP block in the lamellar microdomains, where the daughter lamellae developed from the parent iPP crystals due to the intrinsic property of α -form iPP. This lamellar branching has been observed for iPP homopolymer over a wide range of crystallization conditions, such as crystallization in the melt,⁵⁴ solution,⁵⁵ thin films,⁵⁶ and the sheared region of injection-molded components.⁵⁷ In this study, we further demonstrated that the lamellar branching was also occurred in the lamellae-forming diblock even though the constituent was mediated by the 1D spatial confinement.

Figure 9a–c shows the representative 2D WAXD patterns of the shear-oriented $\text{iPP}_{43}\text{aPS}_{57}^{10,4}$ having been crystallized at a low T_c of 10 °C. Similar scattering patterns were observed for crystallization at lower T_c s. The WAXD patterns displayed isotropic rings in tangential-, radial-, and top-view patterns, signaling that the iPP crystals were randomly oriented in the microdomains. This random orientation is believed to arise

from the extremely high nucleation density at large undercoolings. When a given nucleus appears within the lamellar microdomain, it should not feel the confinement effect because its dimension is much smaller than the lamellar thickness; consequently, most nuclei developed in the microdomain are randomly oriented. At very large undercooling (T_c lower than 10 °C in present case), where the nucleation is extremely rapid, a great number of nuclei explode in the microdomain abruptly; therefore, the microdomains are quickly filled with randomly oriented nuclei, and the crystal growth becomes highly frustrated by the jamming of these crystallites, leading eventually to crystals in random orientation. This result was consistent with the previous findings for other PE-, PEO-, PCL-, and PLLA-containing C-A diblock copolymers crystallized at large undercooling.^{31–33,38,40}

4. CONCLUSIONS

The crystallization behavior and crystalline morphology of the stereoregular diblock copolymer iPP-*b*-aPS have been studied in detail. The iPP blocks in the copolymers under study formed lamellar, cylindrical, and spherical microdomains in the melt. The crystallization kinetics of iPP was strongly affected by the microdomain morphology, which was associated with the alteration of the nucleation mechanism. Moreover, the correlation among the confinement geometry, the nucleation mechanism, and the length scales of the crystal growth has been established by implementing the self-nucleation experiment. It was found that the crystallization in the isolated cylindrical and spherical microdomains was associated with homogeneous nucleation and highly frustrated crystal growth, leading to different self-nucleation behavior in Domain II and Domain III as compared with the results when crystallization was initiated by the heterogeneous nucleation. For the local chain conformation of iPP, it was found that the disruption of a longer helical sequence was mainly dependent on the temperature but not on the microdomain morphology. This indicated that the population of the helical sequence was essentially unperturbed by the global chain stretching induced by formation of microdomains. The orientation of iPP crystals revealed by 2D SAXS/WAXD showed that the crystals formed at a relatively low temperature ($T_c \leq 10$ °C) were randomly orientated, whereas a special lamellar branching of α -form iPP was observed at higher T_c (ranging from 15 to 80 °C) in the lamellar microdomains, consisting of parent and daughter lamellae. The crystalline stems in the parent crystals aligned perpendicularly to the lamellar interface, while the daughter lamellae developed from the parent crystals with a specific angle of 80° or 100°, arising from the intrinsic property of molecular epitaxy.

■ ASSOCIATED CONTENT

■ Supporting Information

¹H NMR spectrum of iPP₃₄aPS₆₆^{11.6}; GPC elution curve of iPP₃₄aPS₆₆^{11.6}; TEM micrograph of iPP₃₄aPS₆₆^{11.6} after quenching from the melt to room temperature; DSC cooling and subsequent heating scans at 10 °C/min after self-nucleation of iPP₂₃aPS₇₇^{17.8} at the indicated self-nucleation temperatures (T_s); the self-nucleation domains for the iPP block within iPP₂₃aPS₇₇^{17.8}; the IR spectra of iPP₄₃aPS₅₇^{10.4} and aPS homopolymer collected at 30 °C. This material is available free of charge via the Internet at <http://pubs.acs.org>.

■ AUTHOR INFORMATION

Corresponding Author

*E-mail: hlchen@che.nthu.edu.tw.

Notes

The authors declare no competing financial interest.

■ ACKNOWLEDGMENTS

We gratefully appreciate Professor Bernard Lotz (Institut Charles Sadron, Strasbourg) and Professor Chien-Lung Wang (National Chiao Tung University, Hsinchu, Taiwan) for the valuable discussions regarding the orientations of α - α branching of iPP crystals in the lamellar microdomains. Professor Feng-Chih Chang and Dr. Shih-Chien Chen at National Chiao Tung University for the assistance in the FTIR experiment are highly appreciated. We would also like to thank the National Synchrotron Radiation Research Center for supporting the X-ray scattering experiments at beamline BL23A1 and BL17A1. Finally, we acknowledge the supports of the National Science Council, Taiwan, under Grant NSC 99-2221-E-007-008 and the Frontier Center of Fundamental and Applied Sciences of Matters of the National Tsing Hua University.

■ REFERENCES

- (1) Bates, F. S.; Fredrickson, G. H. *Annu. Rev. Phys. Chem.* **1990**, *41*, 525–557.
- (2) Bates, F. S.; Fredrickson, G. H. *Phys. Today* **1999**, *52*, 32–38.
- (3) Leibler, L. *Macromolecules* **1980**, *13*, 1602–1617.
- (4) Weimann, P. A.; Hajduk, P. A.; Hajduk, D. A.; Chu, C.; Chaffin, K. A.; Brodil, J. C.; Bates, F. S. *J. Polym. Sci., Part B: Polym. Phys.* **1999**, *37*, 2053–2068.
- (5) Müller, A. J.; Balsamo, V.; Arnal, M. L.; Jakob, T.; Schmalz, H.; Abetz, V. *Macromolecules* **2002**, *35*, 3048–3058.
- (6) Ho, R. M.; Lin, F. H.; Tsai, C. C.; Lin, C. C.; Ko, B. T.; Hsiao, B. S.; Sics, I. *Macromolecules* **2004**, *37*, 5985–5994.
- (7) Castillo, R. V.; Müller, A. J.; Lin, M. C.; Chen, H. L.; Jeng, U. S.; Hillmyer, M. A. *Macromolecules* **2008**, *41*, 6154–6164.
- (8) Nandan, B.; Hsu, J. Y.; Chen, H. L. *J. Macromol. Sci., Part C: Polym. Rev.* **2006**, *46*, 143–172.
- (9) Nojima, S.; Kato, K.; Yamamoto, S.; Ashida, T. *Macromolecules* **1992**, *25*, 2237–2242.
- (10) Rangarajan, P.; Register, R. A.; Fetters, L. J.; Naylor, S.; Ryan, A. J. *Macromolecules* **1995**, *28*, 1422–1428.
- (11) Hamley, I. W.; Fairclough, J. P. A.; Terrill, N. J.; Ryan, A. J.; Lipic, P. M.; Bates, F. S.; Towns-Andrews, E. *Macromolecules* **1996**, *29*, 8835–8843.
- (12) Zhu, L.; Chen, Y.; Zhang, A.; Calhoun, B. H.; Chun, M.; Quirk, R. P.; Cheng, S. Z. D.; Hsiao, B. S.; Yeh, F.; Hashimoto, T. *Phys. Rev. B* **1999**, *60*, 10022–10031.
- (13) Chen, H. L.; Hsiao, S. C.; Lin, T. L.; Yamauchi, K.; Hasegawa, H.; Hashimoto, T. *Macromolecules* **2001**, *34*, 671–674.
- (14) Chen, H. L.; Wu, J. C.; Lin, T. L.; Lin, J. S. *Macromolecules* **2001**, *34*, 6936–6944.
- (15) Hsu, J. Y.; Hsieh, I. F.; Nandan, B.; Chiu, F. C.; Chen, J. H.; Jeng, U. S.; Chen, H. L. *Macromolecules* **2007**, *40*, 5014–5022.
- (16) Kuo, J. C.; Lin, W. F.; Yu, C. H.; Tsai, J. C.; Wang, T. C.; Chung, T. M.; Ho, R. M. *Macromolecules* **2008**, *41*, 7967–7977.
- (17) Lotz, B.; Wittmann, J. C.; Lovinger, A. J. *Polymer* **1996**, *37*, 4979–4992.
- (18) Kobayashi, M.; Akita, K.; Tadokoro, H. *Makromol. Chem.* **1968**, *118*, 324–342.
- (19) Kissin, Y. V.; Rishina, L. A. *Eur. Polym. J.* **1976**, *12*, 757–759.
- (20) Zhu, X. Y.; Yan, D. Y.; Yao, H. X.; Zhu, P. F. *Macromol. Rapid Commun.* **2000**, *21*, 354–357.
- (21) Zhu, X. Y.; Yan, D. Y. *Macromol. Chem. Phys.* **2001**, *202*, 1109–1113.

- (22) Yang, Y. W.; Tanodekaew, S.; Mai, S. M.; Booth, C.; Ryan, A. J.; Bras, W.; Viras, K. *Macromolecules* **1995**, *28*, 6029–6041.
- (23) Hong, S.; Yang, L. Z.; MacKnight, W. J.; Gido, S. P. *Macromolecules* **2001**, *34*, 7009–7016.
- (24) Lin, M. C.; Wang, Y. C.; Chen, J. H.; Chen, H. L.; Müller, A. J.; Su, C. J.; Jeng, U. S. *Macromolecules* **2011**, *44*, 6875–6884.
- (25) Sun, Y. S.; Chung, T. M.; Li, Y. J.; Ho, R. M.; Ko, B. T.; Jeng, U. S.; Lotz, B. *Macromolecules* **2006**, *39*, 5782–5788.
- (26) Douzinas, K. C.; Cohen, R. E. *Macromolecules* **1992**, *25*, 5030–5035.
- (27) Kofinas, P.; Cohen, R. E. *Macromolecules* **1994**, *27*, 3002–3008.
- (28) Lin, M. C.; Wang, Y. C.; Chen, H. L.; Müller, A. J.; Su, C. J.; Jeng, U. S. *J. Phys. Chem. B* **2011**, *115*, 2494–2502.
- (29) Lin, M. C.; Nandan, B.; Chen, H. L. *Soft Matter* **2012**, *8*, 7306–7322.
- (30) Zhu, L.; Cheng, S. Z. D.; Calhoun, B. H.; Ge, Q.; Quirk, R. P.; Thomas, E. L.; Hsiao, B. S.; Yeh, F. J.; Lotz, B. *J. Am. Chem. Soc.* **2000**, *122*, 5957–5967.
- (31) Sun, Y. S.; Chung, T. M.; Li, Y. J.; Ho, R. M.; Ko, B. T.; Jeng, U. S. *Macromolecules* **2007**, *40*, 6778–6781.
- (32) Huang, P.; Zhu, L.; Guo, Y.; Ge, Q.; Jing, A. J.; Chen, W. Y.; Quirk, R. P.; Cheng, S. Z. D.; Thomas, E. L.; Lotz, B.; Hsiao, B. S.; et al. *Macromolecules* **2004**, *37*, 3689–3698.
- (33) Hsiao, M. S.; Zheng, J. X.; Horn, R. M. V.; Quirk, R. P.; Thomas, E. L.; Chen, H. L.; Lotz, B.; Cheng, S. Z. D. *Macromolecules* **2009**, *42*, 8343–8352.
- (34) Hsiao, M. S.; Zheng, J. X.; Leng, S. W.; Van Horn, R. M.; Quirk, R. P.; Thomas, E. L.; Chen, H. L.; Hsiao, B. S.; Rong, L. X.; Lotz, B.; et al. *Macromolecules* **2008**, *41*, 8114–8123.
- (35) Hasan, T.; Ioku, A.; Nishii, K.; Shiono, T.; Ikeda, T. *Macromolecules* **2001**, *34*, 3142–3145.
- (36) Tsai, J. C.; Ho, R. M.; Kuo, J. C.; Lin, W. F.; Yu, C. H.; Wang, T. C.; Chung, T. M. *Macromolecules* **2008**, *41*, 7967–7977.
- (37) Han, C. J.; Lee, M. S.; Byun, D. J.; Kim, S. Y. *Macromolecules* **2002**, *35*, 8923–8925.
- (38) Fillon, B.; Wittman, J. C.; Lotz, B.; Thierry, A. *J. Polym. Sci., Part B: Polym. Phys.* **1993**, *31*, 1383–1393.
- (39) Jeng, U. S.; Su, C. H.; Su, C. J.; Liao, K. F.; Chuang, W. T.; Lai, Y. H.; Chang, J. W.; Chen, Y. J.; Huang, Y. S.; Lee, M. T.; et al. *J. Appl. Crystallogr.* **2010**, *43*, 110–121.
- (40) Tanaka, H.; Hasegawa, H.; Hashimoto, T. *Macromolecules* **1991**, *24*, 240–251.
- (41) Khandpur, A. K.; Forster, S.; Bates, F. S.; Hamlet, I. W.; Ryan, A. J.; Bras, W.; Almdal, K.; Mortensen, K. *Macromolecules* **1995**, *28*, 8796–8806.
- (42) Matsen, M. W.; Bates, F. S. *Macromolecules* **1996**, *29*, 1091–1098.
- (43) Lynd, N. A.; Hillmyer, M. A. *Macromolecules* **2005**, *38*, 8803–8810.
- (44) Court, F.; Hashimoto, T. *Macromolecules* **2001**, *34*, 2536–2545.
- (45) Chen, F.; Kondo, Y.; Hashimoto, T. *Macromolecules* **2007**, *40*, 3714–3723.
- (46) Arnal, M. L.; Matos, M. E.; Morales, R. A.; Santana, O. O.; Müller, A. J. *Macromol. Chem. Phys.* **1998**, *199*, 2275–2288.
- (47) Arnal, M. L.; Müller, A. J.; Maiti, P.; Hikosaka, M. *Macromol. Chem. Phys.* **2000**, *201*, 2493–2504.
- (48) Balsamo, V.; Paolini, Y.; Ronca, G.; Müller, A. J. *Macromol. Chem. Phys.* **2000**, *201*, 2711–2720.
- (49) Burfield, D. R.; Loi, P. S. T. *J. Appl. Polym. Sci.* **1988**, *36*, 279–293.
- (50) Sikka, S. *Mater. Sci. Eng.* **1979**, *41*, 265–269.
- (51) Rubinstein, M.; Colby, R. H. *Polymer Physics*; Oxford University Press: New York, 2003; Chapters 2.6 & 3.2.
- (52) Natta, G.; Corradini, P. *Nuovo Cimento Suppl.* **1960**, *15*, 40–51.
- (53) Lotz, B.; Wittmann, J. C. *J. Polym. Sci., Part B: Polym. Phys.* **1986**, *24*, 1541–1558.
- (54) Binsbergen, F. L.; de Lange, B. G. M. *Polymer* **1968**, *9*, 23–40.
- (55) Khoury, F. J. *Res. Natl. Bur. Stand., Sect. A* **1966**, *70A*, 29–61.
- (56) Padden, F. J.; Keith, H. D. *J. Appl. Phys.* **1973**, *44*, 1217–1223.
- (57) Fujiyama, M.; Wakino, T.; Kawasaki, Y. *J. Appl. Polym. Sci.* **1988**, *35*, 29–49.